A Study on Brushless PM Slotless Motor with Toroidal Winding

Ho-Young Lee[1], Eui-Chun Lee[1], Soon-O Kwon[1], Jung-Pyo Hong[2]
[1]Department of Technology Convergence Group, Korea Institute of Industrial Technology, Daegu, South Korea
[2]Department of Automotive Engineering, Hanyang University, Seoul 133-791, South Korea

***Abstract*—This paper presents a study on brushless permanent magnet (PM) slotless motor with toroidal winding (TWSL). Herein, slotted motor with conventional winding (i.e., CWS motor), which has already been applied to the industry, is compared to the TWSL motor. A finite-element analysis is used to comprehend the operation basis of the TWSL motor, including the linkage flux, back electromotive force, and torque. The proposed TWSL motor can generate the torque level as much as the CWS motor does. The proposed TWSL motor is manufactured and experimented upon to validate the finite-element analysis result.**

Keywords— slotless motor, toroidal winding, surface mounted permanent-magnet motor (SPM), cogging torque, slotted motor, brushless PM motor, torque ripple

I. INTRODUCTION

The noise regulation of automobile parts has much been strengthened by the gradual enlargement of the electric vehicle market. Accordingly, the actuators mounted on automobiles have changed from the brushed DC motor to the brushless DC motor (BLDC) because of the high efficiency, power density, long lifetime, and low mechanical noise in the absence of a commutator. However, the BLDC motor exhibits inevitably cogging torque and ripple because of the interaction between the permanent magnet (PM) and the core teeth of the slotted stator [1]. The cogging torque can be important in terms of the noise and vibration as well as the smoothness in the rotor rotation [2]. Various methods to minimize the cogging torque, such as skewing lamination and magnet, special core shape, and electric compensation in the motor controller, were developed in the past years [3–5]. Nevertheless, these technologies cannot eliminate the cogging torque to near zero like the slotless motor does [6, 7]. Moreover, it is difficult for the slotted stator of the BLDC to wound the coil in a small-sized motor and prevent the minimization of the motor's overall size. Some of the advantages of the slotless motor compared with the slotted motor are [8–10]:.

1) zero-cogging torque for a smooth operation;
2) easy cooling of the generated heat from the winding placed in the air gap; and
3) small inductance compared to the slotted motors and more accurate sensor-less driving possible.

Special thanks to Infolitica Magnet(V7.7) electo-magnetic simulation software and DONG-AH. Co. Ltd.

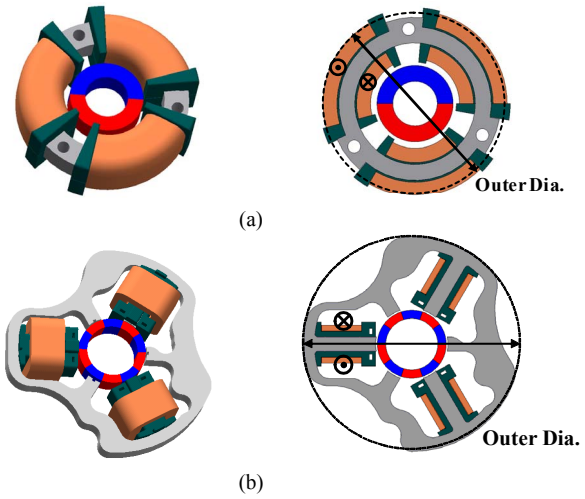

Fig. 1. Basic setup and configuration in 3D schematic: (a) TWSL motor and (b) CWS motor.

In other words, the slotless BLDC motor is suitable for the automotive actuator requiring a compact size and a silent drive. It also undergoes a difficult winding process, which demands a special winding jig or a non-magnetic material for wire arrangement [11]. Therefore, this study proposes a slotless BLDC motor structure with the toroidal winding, which does not use a special winding jig. The winding process of TWSL motor is simpler then conventional slotless motor.

II. MOTOR TOPOLOGY AND CHARACTERISTICS

A. Proposed configuration

The proposed slotless motor structure consists of the ring-type stator wounded with a three-phase toroidal winding and a rotor mounted with a 2-pole rare-earth permanent magnet (Fig. 1(a)). The CWS motor, which had already applied to the industry, is presented for comparison (Fig. 1(b)). This structure consists of a six-slot stator wounded with a three-phase conventional winding and a rotor mounted with a 10-pole permanent magnet. Table I shows the TWSL and CWS motor specifications.

978-1-5090-4281-4/17/$31.00 ©2017 IEEE

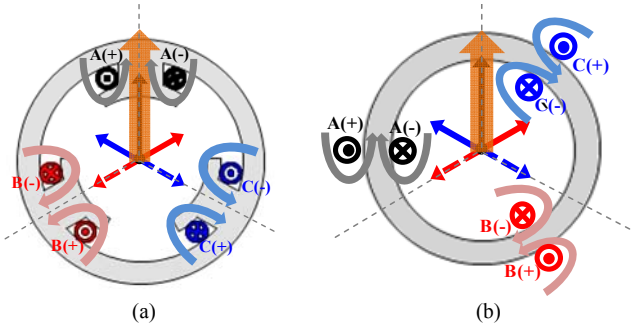

(a) (b)

Fig. 2. Flux distribution and magnetomotive force by the winding: (a) TWSL motor and (b) CWS motor.

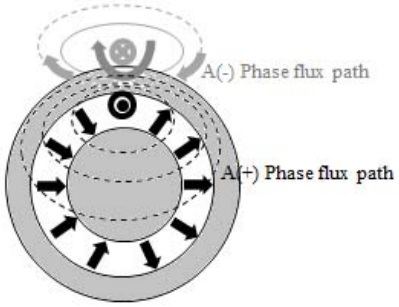

Fig. 3. Flux distribution by one phase of the TWSL motor.

B. *Flux distribution by winding*

Fig. 2(a) shows the three-phase windings installed 120° apart at the stator teeth of the general slot motor. The resultant magnetomotive force is of a constant magnitude and rotates in the counterclockwise direction when an alternating current is applied.

The slotless motor proposed in the present study has a winding structure, in which the coils are wound in the theta direction along the stator yoke (Fig. 2(b)). As a result, the coil side is arranged inside and outside of the stator yoke. As shown in Fig. 2(b), the flux created in the coil located outside the stator is not introduced inside the stator; hence, it practically does not contribute to the creation of a rotating magnetic field. A rotating magnetic field is ultimately created because of the three-phase coils located inside the stator. A rotor with polarity is then rotated by the force to align with this rotating magnetic field.

As shown in Fig. 3, the magnetomotive force at the air gap can be calculated by applying the Ampere's Circuit Law in the closed circuit made by the magnetic flux path produced by the a-phase windings. Assuming that the permeability of the iron core is infinite, only the magnetic field component in the normal direction is left in the core boundary surface. The magnetomotive force in the air gap at the P-pole is expressed in Eq. (1) as follows:

$$F_a = \frac{H_g l_g}{2p} = \frac{N}{P} i_a(\mathrm{t}) = \frac{N}{P}\sqrt{2} I \cos \omega_e t \tag{1}$$

where H_g is a magnetic field at the air gap; l_g is the length of the air gap; p is the number of pole pairs; N is the number of coil turns; ω_e is an electrical frequency; and i_a is a phase current. A spatial distribution of the magnetomotive force in the concentrated winding becomes a square wave expressed in Eq. (2) at the ideal condition:

$$f_a = \frac{4}{\pi} F_a \left(\sin\theta + \frac{1}{3}\sin 3\theta + \frac{1}{5}\sin 5\theta + \cdots + \frac{1}{v}\sin v\theta \right) \tag{2}$$

where v is a harmonic order. The fundamental component in the magnetomotive force is expressed in Eq. (3).

TABLE I. TWSL AND CWS MOTOR SPECIFICATIONS

Quantity		Motor type	
		TWSL	***CWS***
Dimension	Outer diameter [mm]	29	38
	Rotor outer diameter [mm]	12	12
	Rotor inner diameter [mm]	7	9
	Magnetic air-gap [mm]	3.5	0.3
	Stack length [mm]	4.5	4.5
	Pole/slot number	10/6	2/-
Winding	Coil bulk number	3	3
	Turn number [t]	600	586
	Coil diameter [mm]	0.15	0.11
Material	Remanence of magnet [T]	1.2	0.5
	Core	50PN1300	

By substituting Eq. (3) into Eq. (1), a distribution of the single-phase magnetomotive force that is temporally and spatially changed can be obtained by Eq. (4):

$$f_{a1} = \frac{4}{\pi} F_a \sin\theta \tag{3}$$

$$f_{a1} = \frac{4}{\pi}\frac{N}{P}\sqrt{2} I \cos\omega_e t \cdot \sin\theta = F_m \cos\omega_e t \cdot \sin\theta \tag{4}$$

A distribution of the magnetomotive force in the a, b, and c phases after applying the trigonometric formula to Eq. (4) is presented by Eqs. (5), (6), and (7), respectively, as follows:

$$f_{a1} = \frac{F_m}{2}\sin(\theta - \omega_e t) + \frac{F_m}{2}\sin(\theta + \omega_e t) \tag{5}$$

$$f_{b1} = \frac{F_m}{2}\sin(\theta - \omega_e t) + \frac{F_m}{2}\sin(\theta + \omega_e t - 240) \tag{6}$$

$$f_{c1} = \frac{F_m}{2}\sin(\theta - \omega_e t) + \frac{F_m}{2}\sin(\theta + \omega_e t - 120) \tag{7}$$

The magnetomotive force distribution in the air gap is the sum of the magnetomotive forces in the a, b, and c phases. The resultant magnetomotive force can be expressed by Eq. (8) as:

$$f_1 = f_{a1} + f_{b1} + f_{c1} = \frac{3}{2} F_m \sin(\theta - \omega_e t) \tag{8}$$

The resultant magnetmotive force of three phase has an amplitude of $1.5F_m$. The magnetomotive force, which is spatially sinusoidal, is rotated in the counterclockwise direction.

C. Back-EMF by the magnet

Using FEM, the flux linkage waveform shown in Fig. 5 illustrates that the associated back electromotive force (EMF) is the derivative of the waveform as dictated by Faraday's law. The total linkage flux becomes zero because the outgoing and incoming linkage fluxes at the a-phase winding are the same at locations, where the rotor is positioned at 0° and 180° (Fig. 4). The back-EMF has a sinusoidal wave shape (Fig. 5) and is given as follows [12]:

$$e_a = \frac{d\lambda}{dt} = \frac{d\theta_e}{dt}\frac{d\lambda}{d\theta_e} = \omega_e \frac{d\lambda}{d\theta_e}$$

$$= \frac{N_m}{2}\omega_m \frac{d\lambda}{d\theta_e} = \frac{N_m}{2}\omega_m \frac{2N\phi_g}{\pi} \tag{9}$$

where λ is the flux linkage; ω_m is the angular velocity in radM/s; θ_e and θ_m are the electrical and mechanical angles, respectively; and N_m and N are the number of the magnet poles and the turns of the winding, respectively. The air gap flux can be written as follows for further simplification:

$$\phi_g = B_g A_g = B_g R_{ro} \theta_p L_{st} = \frac{2\pi}{N_m} B_g L_{st} R_{ro} \tag{10}$$

where B_g is the air gap flux density; θ_p is the angular pole pitch in radM; R_{ro} is the air gap radius at the magnet surface; and L_{st} is the axial length of the motor. Substituting this relationship into Eq. (9) yields the amplitude of the back-EMF as [13]:

$$|e_a| = \frac{N_m}{2}\omega_m \frac{2N}{\pi}\left(\frac{2\pi}{N_m} B_g L_{st} R_{ro}\right)$$

$$= 2NB_g L_{st} R_{ro} \omega_m = K_e \omega_m \tag{11}$$

This expression agrees with the *BLV* law. The factor $2N$ is caused by to the two slots each having an N conductor.

As shown on the right in Eq. (11), all terms in this expression, except for the ω_m, form a *back-EMF constant*, *Ke*, whose units are V/(radM/s).

The phase back-EMF and its total harmonic distortion (THD) in the general slot motor and the slotless motor are compared using FEM. The phase back-EMF at 600 RPM is 0.211 Vrms and 0.320 Vrms, showing that the slotless motor provided an approximately 44% higher phase back-EMF than the general motor. However, the coils in the proposed slotless motor are wound in the air gap area. Hence, the air gap in the slotless motor is much larger than that of the slot-type motor. The slotless model proposed in this study employs more magnets and higher-grade magnets (Table 1). The THDs of the back-EMFs are 0.06% and 12.9%, indicating that the THD of the slotless motor is significantly lower than that of the slot-type motor. Furthermore, the cogging torque is zero, theoretically, because the slotless motor has no teeth shape in the stator.

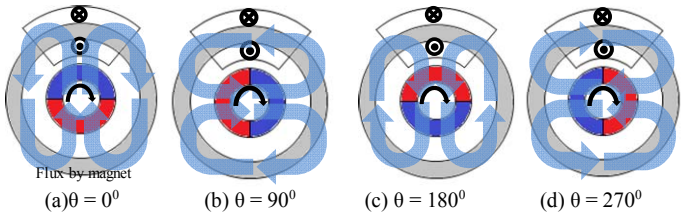

Fig. 4. Flux path by the magnet. Rotor angle: (a) 0^0, (b) 90^0,(c) 180^0, and (d) 270^o.

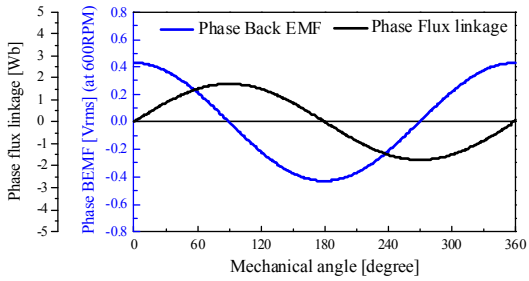

Fig. 5. Phase flux linkage and back EMF in the no-load condition using the finite-element method.

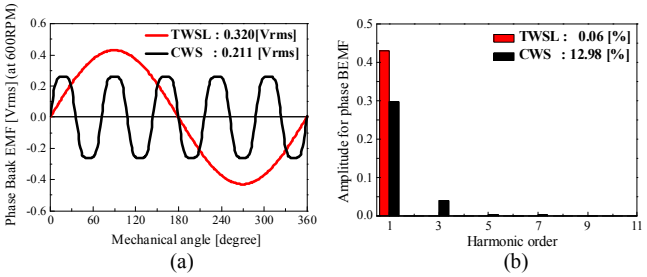

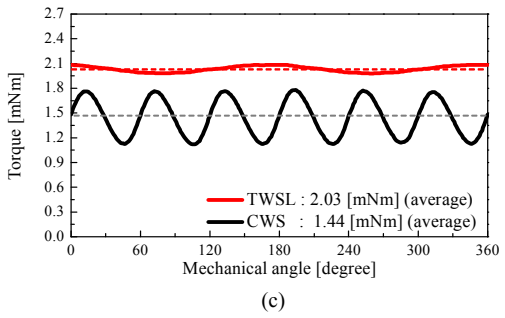

Fig. 6. Finite element method result : (a) phase back EMF, (b) total harmonic distortion, and (c) torque.

Thus, the slotless type is much more advantageous than the slot type in terms of the vibration noise.

D. Torque

The power input in an idealized machine is equal to the power output, as shown in Eq. (12):

$$P_{\text{in}} \approx P_{out} = T\omega_m = ei \tag{12}$$

where P_{in} and P_{out} are the electrical input power and the mechanical output power, respectively. Thus, from Eqs. (11) and (12), the torque amplitude can be expressed as follows [13]:

$$|T| = \frac{ei}{\omega_m} = 2NB_g L_{st} R_{ro} i = K_t i \tag{13}$$

All terms in this expression, except for R_{ro}, represent the force experienced by the rotor. This force acting at the radius R_{ro} provides the torque. From a different point of view, all terms in Eq. (13), except for i, form a *torque constant kt*, whose units are N·m/A.

A load analysis was conducted using the finite-element method (FEM) to compare the torque and the torque ripple between the two models. The current condition is as follows: the phase current is 0.2 Arms, while the applied current phase angle is the same as the phase of the back-EMF. As a result, the slot type has a mean torque of 1.44 [mNm], whereas the slotless type had 2.03 [mNm]. As presented in Eq. (13), a torque is generated proportional to the back-EMF magnitude when the same current is applied. Thus, the slotless model generates approximately 41% higher torque than the slot model. The torque ripple is calculated using Eq. (14). The calculation result shows that the torque ripple in the slot type is 45.8 [%], whereas that in the slotless type is 5.4 [%].

$$T_{ripple} = \frac{T_{\max} - T_{\min}}{T_{ave}} \times 100 \tag{14}$$

where $T_{\max}$ and $T_{\min}$ are the maximum and minimum torque, respectively; and T_{ave} is the average torque that resulted from the load FEM. Similar to that in the THD result, the slotless type is more advantageous than the slot type in terms of the vibration noise.

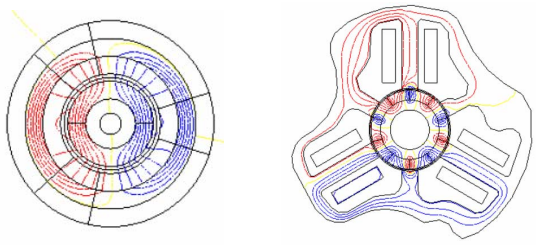

(a) (b)

Fig. 7. Equivalent potential line at the load condition: (a) TWSL and (b) CWS.

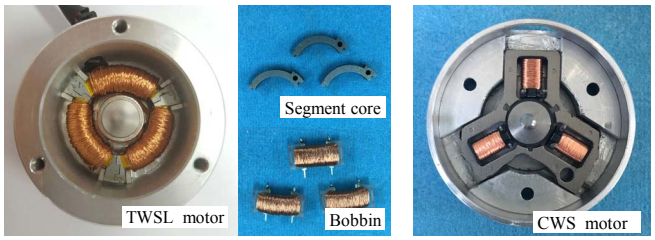

(a) (b)

Fig. 8. Prototype of the assembled TWSL and CWS motor: (a) proposed TWSL motor and (b) CWS motor.

III. PROTOTYPE MANUFACTURE AND TESTING

A. Manufacture

Fig. 8 shows the prototype of the assembled TWSL motor and the CWS motor. The stator core of the TWSL motor is divided into a three-segment core to facilitate coil winding. The bobbins wounded at the 0.15 mm coil diameter and 600 turn are assembled with the segment core and connected. The rotor consists of the ring-type rare-earth permanent magnet and the shaft of a non-magnetic material.

B. Testing

Fig. 9 shows the phase back-EMF tests of the manufactured TWSL and CWS motor at 600 r/min. Even though the winding is completed by hand, the values of the EMFs are very similar. The measured back-EMF of the TWSL motor is 0.302 Vrms, showing a good agreement compared with the predicted 0.320 Vrms by the FEM. The back-EMFs of the CWS motor are also similar.

The manufactured TWSL motor is connected to the torque measuring system (Fig. 10(a)). The measurement equipment consists of a DC power supply, a dynamometer for estimating the output characteristics, a power meter for calculating the input power, and a laptop computer for load control (Fig. 10(b)). Fig. 10(c) shows the dynamo loading test result for the TWSL motor and the CWS motor.

The two models are measured with the same controller during the dynamo loading test. However, the controller is not optimized in the proposed 2-pole slotless-type model because it applies to the existing 10-pole slot-type models. The dynamo loading test results show that the slotless model has an approximately 10% higher input current than the slot model at the same load torque of 2.0 mNm. Even if the slotless model

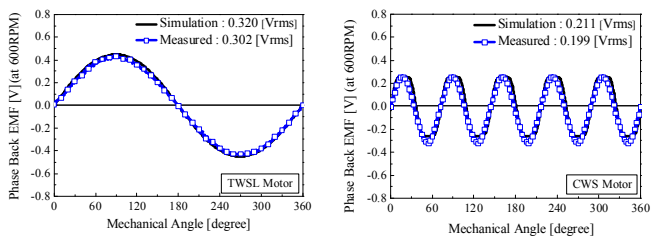

(a) (b)

Fig. 9. Test result of phase back EMF (a) TWSL. (b) CWS.

previously has an approximately 50% higher phase back-EMF in the no-load back-EMF test, it has a higher current applied because of the control of the current phase angle in the non-optimized controller. Table II shows the dynamo experiment results and the performance comparison of the two types.

As described earlier, the proposed slotless model is a motor with clearly distinct advantages and disadvantages. The slotless type has a larger air gap than the slot type. Moreover, the coil side located outside of the stator yoke does not affect the electrical performance, as described in Section B in Chapter II. Thus, the slotless type has the following disadvantages: it needs a larger number of turns, magnets, or higher-grade magnets to achieve the same performance with the slot type. However, the cogging torque, THD, and torque ripple are much lower than those in the slot type because the teeth and the slot structure are not present in the stator due to the slotless structure. Furthermore, the *torque per current per motor volume* in the slotless model is much higher than that of the slot model (Table II). These results denote that compared to the slotted model, the slotless model is a much more appropriate model in fields, where compact size and quiet and noiseless motor running are required.

IV. CONCLUSION

This study proposed a structure for the brushless PM slotless motor with a toroidal winding. The slotted motor with a conventional winding was also presented for comparison and applied to a vehicle's conditioner system. The finite-element method (FEM) was used to comprehend the operation basis of the TWSL motor, such as the linkage flux, back-EMF, and torque. The TWSL motor had a sinusoidal back-EMF wave form with a phase difference of 120°. The average torque was generated at 2.06 mNm when the current 0.243 A of the requirement system was inputted. Finally, the proposed TWSL motor was manufactured and experimented upon to validate the result of the finite element methods, including the back-EMF and torque. In conclusion, the proposed structure of the TWSL motor can generate the torque level as much as the slotted motor with a conventional winding does. The TWSL motor also had advantages of reducing the vibration and noise and minimizing the overall motor size. For reference, the shape design, including the air gap and the coil and stator diameter, of the proposed TWSL motor have yet been optimized, thereby affording a decrease of the dimension and providing margins for improvement.

TABLE II. PERFORMANCE COMPARISON OF THE TWSL AND THE CWS MOTOR

	Quantity	Motor type	
		TWSL	***CWS***
Requirement	Supply voltage [V]	12	
	Operating speed [rpm]	625	
	Operating load torque [mNm]	2.0	
Test result	Direct current [A] (at 2.0 mNm)	0.23	0.21
	Back-EMF [Vrms] (at 600rpm)	0.30	0.19
	Phase resistance [Ω]	12.7	19.0
Performance	Total harmonic distortion [%]	0.06	12.9
	Torque ripple [%]	5.4	45.8
	Torque per current [mNm/A]	8.69	9.52
	Torque per current per motor volume [Nm/A/m^3]	2925	2355

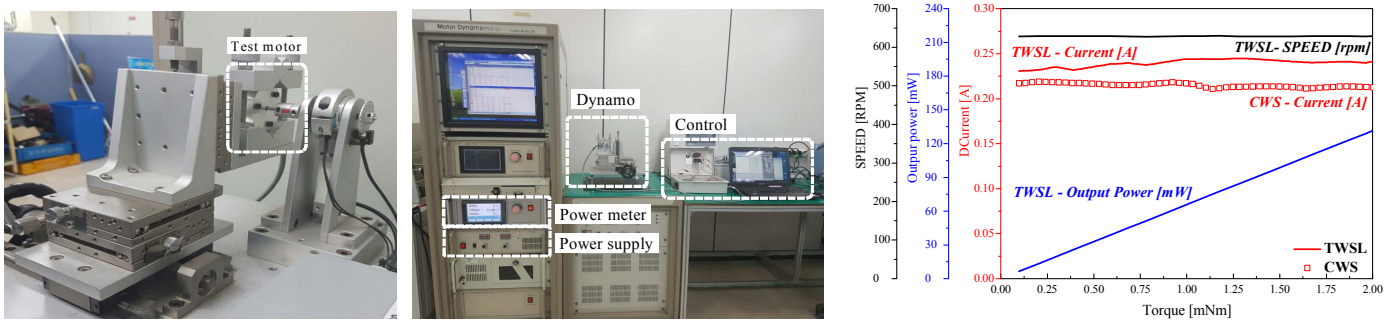

(a) (b) (c)

Fig. 10. Experimental setup and result for the dynamo loading test.
(a) Dynamo. (b) Dynamo loading test with the DC power supply, dynamo, power meter and laptop computer. (c) Dynamo loading test result.

ACKNOWLEDGMENT

Special thanks to Infolitica MagNet (V7.7) electro-magnetic simulation software and DONG-AH.Co.,Ltd.

REFERENCES

[1] J. Xintong, X. Jingwei, L. Yong, L. Yongping, "Theoretical and simulation analysis of influences of stator tooth width on cogging torque of BLDC motors" IEEE Tra. Mag., Vol. 45, No. 10, Oct. 2009

[2] Hong-Seok Ko, Kwang-Joon Kim, "Characterization of noise and vibration sources in interior permanent-magnet brushless DC motors" IEEE Tran. Mag., Vol. 40, No. 6, Nov. 2004.

[3] W. Fei, Z.Q. Zhu, "Comparison of cogging torque reduction in permanent magnet brushless machines by conventional and herringbone skewing techniques" IEEE Tra. Ener. Conver., Vol. 28, No. 3, Sep. 2013.

[4] Sun-Kwon Lee, Gyu-Hong Kang, Jin Hur, Byoung-Woo Kim, "Stator and rotor shape designs of interior permanent magnet type brushless dc motor for reducing torque fluation," IEEE Tra. Mag., Vol. 48, No. 11, Nov. 2012

[5] P. Kshirasgar, R. Krishnan, "High-efficiency current excitation strategy for variable-speed nonsinusoidal back-EMF PMSM machines," IEEE Tra. Ind. App., Vol. 48, No. 6, pp. 1875-1889, Nov. 2012

[6] T. Kosaka, N. Matsui, T. Shikayama, R. Oguro "Drive characteristics of slotless PM motor" IEEE Ind. Appl., vol. 2, pp. 894-899, Aug. 2002.

[7] V. Keloth, M. Mijas, P. Thomas, V Menon, "Analysis of cogging torque reduction techniques of a slotless PM BLDC motor," IEEE ICMMD Int. Con. Mag. & Dri., July 2014.

[8] Jung-Moo Seo, Joo-Han Kim, In-Soung Jung, "Design and analysis of slotless brushless dc motor" IEEE Trans. Ind. Appl.,vol. 47, no. 2 Mar. 2011

[9] A. Tessarolo, F. Agnolet, S. Pieri, M. scalabrin, M. Chiara, M. Martin, "Design optimization and testing of high-performance motors:evaluating a compromise between qulity design development and production costs of a halbach-array PM slotless motor," IEEE Ind. App. Mag., Vol. 22, pp. 19-32, Aug. 2016.

[10] D. Todd, K. Y. Lee, "Electric propulsion with the sensorless permanent magnet synchronous motor: model and approach" IEEE Tra. Ener. Conver., vol. 20, No. 4, pp. 818-825, Dec. 2005

[11] I. Szalay, G. Kohlrusz, "Modeling of slotless surface-mounted PM synchronous motor for sensorless applications," IEEE Int. Ele. Veh. Con., Dec. 2014

[12] Gordon R. Slemon "Electric Machine and Drives" Addison-Wesley, 1992, p90-91

[13] Dr. Duane Hanselman, "Brushless Permanent Magnet Motor Design" The Writer's Collective Cranston, 2003, p76-77